Crossing-link of experimental reducibility tests, XPS characterizations and DFT estimates on ferrite oxygen carriers in CLC

Shuai Liu[a], Zhongbin Dong[d], Dong Xiang[a], Yong Jiang[c], Quanbao Tao[c], Yan Cao[a,b,*]

[a] College of Chemistry & Chemical Engineering, Anhui University, Hefei 230601, PR China
[b] Department of Chemistry, Western Kentucky University (WKU), Bowling Green, KY, 42101, USA
[c] Zhong An United Coal Chemical Co., Ltd, Huainan, PR China
[d] College of Chemical Engineering, Anhui University of Science and Technology, Huainan 232000, PR China

ARTICLE INFO

ABSTRACT

Chemical looping combustion (CLC) is an efficient technology of thermal conversion of carbonaceous fuels with CO_2 being concentrated. Oxygen carriers, which are generally metal oxides or their composites, are critical in the development of different CL processes, addressing combustion, gasification and H_2 production. Iron-based oxide, rich in natural resource and inexpensive, is one of ideal candidates as oxygen carriers in the CL process. Understandings toward the general principles of the selection on iron-based oxygen carriers are highly demanded. A unique approach was applied in the present study to investigate the relationship between the reducibility and the electronic structure of selected three typical ferrites as oxygen carriers, via combining experimental reducibility tests using H_2-TPR and CO-TGA, the material characterizations using XRD (X-ray Diffraction) and XPS (X-ray Photoelectron Spectroscopy), and electronic structures using DFT (Density Functional Theory) calculations. Proportions of the lattice oxygen and Fe^{2+} in ferrites positively and negatively influence their reduction reactivity, respectively. Varieties of oxygen components in ferrites determine their reduction temperatures and reactivity. Both the approaching degrees of the O-2p and M-3d valance bands to Fermi level of ferrites positively influence the initial reducing temperature and the reduction rate, respectively. Using these deeper prediction insights into structure-property relations will greatly increase the success of our subsequent synthetic effort.

1. Introduction

Chemical looping combustion (CLC) is a novel thermal conversion technology of carbonaceous fuels with CO_2 being concentrated [1–4]. In the CLC process, metal oxides act as oxygen carriers that are reduced in the fuel reactor to provide oxygen resource for combustion and then oxidized by air in the air reactor, as shown in Fig. 1 [5]. The CLC technology has shown its promise because it can inherently and efficiently exclude the mixing of N_2 and CO_2, thus concentrating CO_2, and avoid the formation of thermal NO_x in the air reactor [1–4,6]. It is also generally recognized as a high exergy efficiency thermal conversion process [5,6], because oxygen carriers decompose a single reaction into two separated redox reactions [1,6]. In this manner, each reaction step can be ideally configured with the minimized exergy loss of the process 1 and consequently the associated exergy efficiency can be enhanced [1]. Since inception of chemical looping concept, there have currently been new interests in developments of the cost-effectiveness and energy-efficiency of chemical looping processes (CL), such as hydrogen production [7,8], reforming [9,10], gasification [11,12], and selective oxidation [13].

Oxygen carrier is key to the success implement of many chemical looping processes [14–16]. Its selection and synthesis require a thorough knowledge on the intrinsic properties of various promising candidates, such as reactivity and thermal stability [14,17]. Single metal oxide materials were studied extensively, mainly including Fe-, Ni-, Cu-, Co- and Ca-based single oxides [14]. Fe-based oxygen carriers are considered a promising candidate for CL processes due to their richness in natural deposits, low cost, desirable thermodynamic and kinetic properties, satisfactory mechanical strength, and environmental compatibility [14,15,20]. Cu-based oxygen carriers have shown high reaction rates and no thermodynamic restrictions for completely converting fuel to CO_2 and H_2O under proper temperatures, but the low melting point is their weakness [3,14,18–20]. Co-based oxygen carriers are higher in their transport capacity but also costly and environment-

---

* Corresponding author at: College of Chemistry & Chemical Engineering, Anhui University, Hefei 230601, PR China.
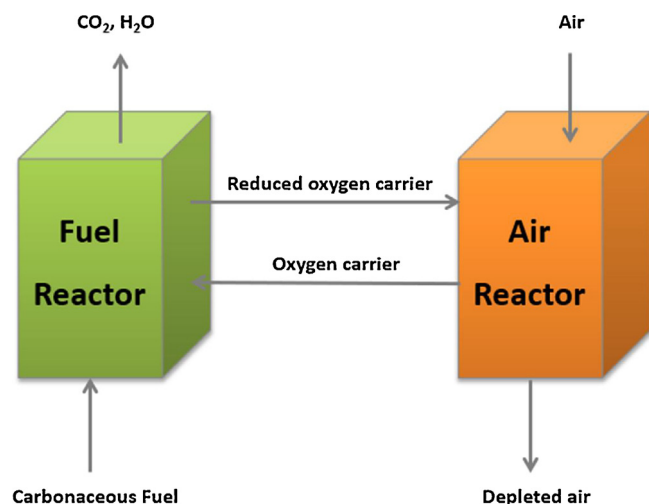 *E-mail address:* yan.cao@wku.edu (Y. Cao).

Fig. 1. Simplified schematic CLC process.

concerned [14]. Both Cu- and Co-based oxygen carriers can achieve chemical looping uncoupling with the direct free oxygen release for use, which is ideal for solid fuel conversions. Ca-based oxygen carriers are widely-accessible, inexpensive and highly reactive under high temperatures, and thus quite attractive in chemical looping processes as both an oxygen carrier via a cycle of CaS-CaSO$_4$ and directly as a CO$_2$ sorbent [21–23].

Further investigations revealed even better properties of complex metal oxide materials than those of single metal oxides, because of synergistic effects on reactivity and selectivity of complex metal oxides [14,24]. Perovskite and spinel structures of complex metal oxides have been recently focused due to their unique advantages [1,2]. Perovskite-type oxygen carriers have a high oxygen diffusivity because of the nonstoichiometric oxygen in their bulk structures to host larger concentrations of oxygen vacancies at elevated temperatures [1,2,24,25]. Spinel has a special structure which is based on a close-packed O^{2-} anion lattice in which metal cations distribute at octahedral and tetrahedral interstitial sites in the lattice [26]. Its non-stoichiometric structure makes the diverse distributions of cations in the lattice and a considerably higher concentration of cation vacancies than oxygen vacancies under oxidative conditions [26–28].

Iron-based spinel or perovskite oxides were generally called metal ferrites, and were interesting for extensive studies. Typically, metal ferrites can be stable under high temperatures [29–31]. For example, the spinel-structured CuFe$_2$O$_4$ and NiFe$_2$O$_4$ promised both high reactivity and thermal stability [15,32]. Most of metal ferrites also have strong magnetic property, as is an attractive feature on the easy separation of oxygen carriers from the solid fuel ash [33,34]. Additionally, the reduced ferrites can react with steam to produce hydrogen, leading to their promising candidates in the chemical looping hydrogen production (CLH) [17,35,36].

The spinel ferrite with a ratio of M/Fe = 1/2 has been paid special attention on their well-performed in the chemical looping process [37,38]. Evdou et al. [33] synthesized a series of spinel ferrite MeFe$_2$O$_4$ (Me = Mn, Ni, Zn, Co and Cu) via solid-state reactions and systematically compared their performances in the CH$_4$ oxidation. They found that CuFe$_2$O$_4$ and CoFe$_2$O$_4$ presented high oxygen transfer capabilities (OTC) and remarkable thermal stabilities. Wang et al. [34] prepared three kinds of metal ferrites (CuFe$_2$O$_4$, NiFe$_2$O$_4$ and CoFe$_2$O$_4$) by the sol-gel combustion method, and found that their reactivity as oxygen carriers decreased in an order of CuFe$_2$O$_4$ > CoFe$_2$O$_4$ > NiFe$_2$O$_4$ in both TGA and fluidized bed experiments using pine sawdust as fuel. Furthermore, CuFe$_2$O$_4$ had a lower initial reaction temperature. Both CuFe$_2$O$_4$ and CoFe$_2$O$_4$ showed remarkable thermal stability. Similarly, the perovskite-type ferrites showed their promising performance in

coal-fired CLC [39]. Most interestingly, Ismail et al. [40] and Chan et al. [41] found that inexpensive Ca$_2$Fe$_2$O$_5$ can be a potentially viable material as oxygen carrier for the hydrogen production.

Therefore, understandings on redox mechanisms of complex metal oxide oxygen carriers are highly demanding at their atomic level. One of recent approaches is the theoretical calculation on the density functional theory (DFT). Wang et al. [42] used DFT to investigate the associated surface reaction path of CH$_4$ on the surface of Fe$_2$O$_3$ as oxygen carrier, and inferred that the oxidation of CH$_4$ was initialized via the surface generating hydroxyl radical, followed by chain reactions of CH$_4$ intermediates toward final products of H$_2$O and CO$_2$. Cheng et al. [43] combined DFT calculations and thermogravimetric analysis to study the adsorption and dissociation of CH$_4$ on the surface of Fe$_2$O$_3$, and revealed that oxygen vacancies on the surface range facilitated the CH$_4$ dissociation. They also addressed other typical transition metals (Mn, Co, Ni, Cu) in the CLC process [44], and observed the morphology evolution in the oxidation experiments. The calculated dissociation energy barriers of O$_2$ on the surfaces of these metal crystals revealed the influence of dissociation and migration of oxygen atom on the morphological evolution of nanostructures. Muhich et al. [45] calculated the barriers of cation diffusion of Fe$_3$O$_4$, and further in CoFe$_2$O$_4$ and NiFe$_2$O$_4$ spinel ferrites, based on both DFT and crystal field theory. The simulated associated hopping pathways revealed mechanical understandings on reactivity during the oxidation stage. The DFT method was also applied to understand positive effects of TiO$_2$ support on the performance improvement of iron-based oxygen carriers in the reduction stage. It's found that a much higher O^{2-} diffusivity and a lower vacancy formation energy were associated with the presence of TiO$_2$ support [46,47].

The previous DFT studies focused on the pathways and energy barriers of radical reactions of the CLC process, leading progressive understandings on the redox reaction mechanism. Currently those practices were not sufficient in giving a direct and systematic guidance on the material selection of oxygen carrier. Time-consuming multi-scale CLC experiments were still necessary. There was a missing relevance on predictive power of theoretical modelling toward the actual performance of oxygen carrier materials. This study tried to initialize the connect among redox experiments, structure characterizations and atomic calculations to extract meaningful information guiding on the selection of oxygen carrier materials and structures. Thus, three typical kinds of bimetallic ferrites (CoFe$_2$O$_4$ and CuFe$_2$O$_4$ and Ca$_2$Fe$_2$O$_5$) were selected as the studied systems here. Experiments were carried out via the preparation using the sol-gel combustion method, and then their reduction reaction were tested using both the temperature programmed reduction (H$_2$-TPR) and the thermogravimetric analysis (CO-TGA). Materials characterizations were conducted using X-ray diffraction (XRD) and X-ray photoelectron spectroscopy (XPS). The optimized DFT calculations focused on electronic structures of these three ferrite systems. This combination approach, to the best of our knowledge, was the first trial about the exploration on structure-property-performance relationships and a general guidance on the selection of ferrites as oxygen carriers.

2. Experimental and computational details

2.1. Ferrites synthesis

A series of ferrites (CuFe$_2$O$_4$, CoFe$_2$O$_4$, and Ca$_2$Fe$_2$O$_5$) were synthesized by the sol-gel combustion method. Nitrates were used as original materials with the stoichiometric molar ratio of M/Fe (1:2 for CuFe$_2$O$_4$ and CoFe$_2$O$_4$, and 1:1 for Ca$_2$Fe$_2$O$_5$). They were dissolved in water and stirred to be the uniform solutions. Citric acid was chosen to be the chelating agent, and then added into solutions. Then ammonia hydroxide was used to adjust the pH of aforementioned solutions to maintain their pHs as 7.5. Subsequently, the obtained solutions were heated to approximate 75 °C until the sol-like matter appeared
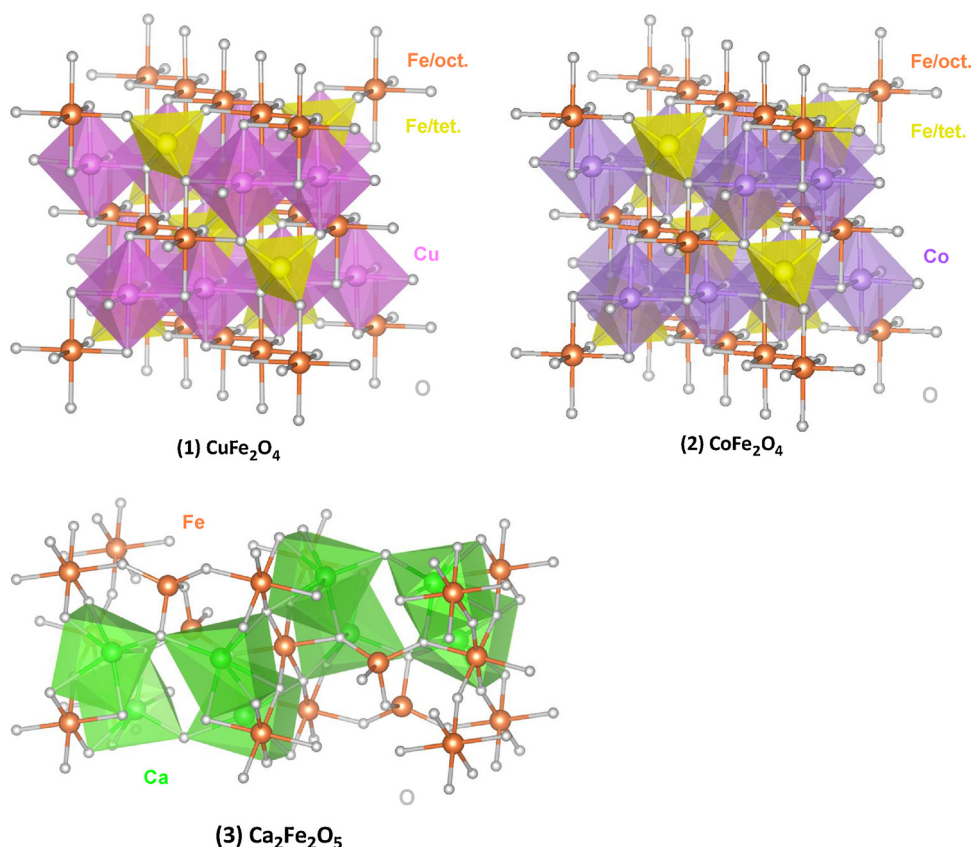
(1) CuFe₂O₄

(2) CoFe₂O₄

(3) Ca₂Fe₂O₅

Fig. 2. DFT calculation systems for (1) $CuFe_2O_4$, (2) $CoFe_2O_4$, and (3) $Ca_2Fe_2O_5$.

(generally 7 h). This was followed by the rising temperature up to 80 °C overnight in an evaporator to obtain the gel-like precursors. The dried precursors were air-calcined to form ferrite crystals in a muffle furnace. The temperature program followed a procedure like: the temperature was firstly increased from 25 to 400 °C with a ramp of 8 °C/min and then remained at 400 °C and then for 2 h, the temperature was continued to rise to 1000 °C at a heating rate of 5 °C/min and finally maintained for 2 h.

2.2. Sample characterizations

The synthesized ferrite samples were characterized by X-ray Diffractometer (XRD, X'Pert-PRO MPD). Scans were performed between 5–80° in every 0.0167° with a time interval of every 10 s. The X-ray source was Cu Kα radiation (λ = 1.54060 Å) with an accelerating voltage at 40 kV and a filament current at 40 mA under room.

X-ray photoelectron spectroscopy (XPS, ESCALAB 250Xi, Thermo Fisher Scientific Inc.) with the X-ray source of Al Kα was employed to explore the charge states, ratios of elements and the valance bands of the whole compound on the surface of the samples. The survey spectra and core-level spectra were recorded under the pass energy of 20 and 100 eV, respectively. The standard C 1s with binding energy of 284.8 eV was selected as a reference.

N₂ adsorption and desorption isotherms were recorded using Micromeritics ASAP2020M + C Analyzer at −196 °C. Prior to nitrogen adsorption the samples were outgassed at 100 °C overnight. The surface area was calculated with the method of Brunauer-Emmett-Teller (BET).

2.3. H₂-TPR and TGA operations

The measurement of H₂-TPR was carried out on a Quantachrome Instrument with a thermal conductivity detector (TCD) for detecting the composition changes of the outlet gas from the reduction of synthesized

ferrites. For each test, 50 mg of samples were loaded in a U-tube reactor to react with 10% H_2/Ar from 40 to 1000 °C at a heating rate of 8 K/min. Argon was used to clean the air out of the reactor before reaction and also to cool the sample after reaction.

Thermogravimetric analysis was conducted on a TGA reactor (STA409C/PC) to investigate the reactivity of samples with CO. In each test, 10 mg of sample was loaded in an alumina crucible and heated from the room temperature to 1150 °C with a heating rate of 10 K/min at the atmosphere of 8% CO/Ar.

2.4. Computational methods

DFT calculations on electronic properties of synthesized ferrites were carried out using a module of Materials studio 7.0 (CASTEP, Cambridge Serial Total Energy Package). Ultra-soft pseudopotentials were introduced to represent the electron-ion interaction for allowing the lowest possible cut-off energy [48]. Generalized Gradient Approximation-Perdew Burke Ernzerhof (GGA-PBE) was selected as exchange-correlation functional in all calculations based on our previous studies [13,49]. An energy cutoff at 680 eV was adopted after a convergence study over the range of 450–750 eV. The k-point separation was specified within 0.02 $Å^{-1}$ in the geometry optimization and 0.04 $Å^{-1}$ in the electronic property calculation, respectively, for balancing calculation accuracy and computational expense.

In the geometry optimization, the convergence criteria for the calculation were set to the energy tolerance at 2.0×10^{-5} eV/atom, the maximum force tolerance at 0.08 eV/Å, the maximum displacement tolerance at 0.002 Å, and the self-consistent field tolerance at 2.0×10^{-6} eV/atom. LDA + U formalism was used in calculations of electronic structures of selected ferrites, considering the highly localized electrons in 3d orbitals and the strong electron correlation in the systems of transition metals [50,51]. Based on our previous study and other references, the value of Hubbard U was set as 4.3 for Fe, 7.5 for
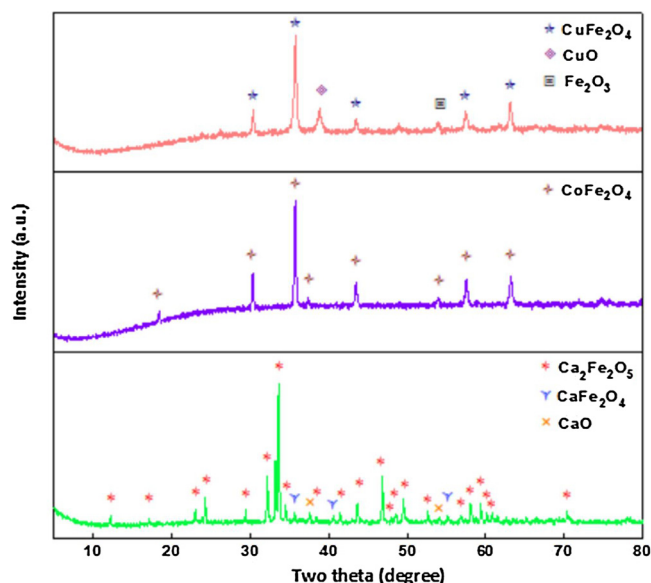
Fig. 3. The XRD spectra of the synthesized ferrite samples.

Cu, and 1.0 for Co. The calculated systems for the three studied samples are shown in Fig. 2.

3. Results and discussion

3.1. XRD characterizations

The XRD characterizations of synthesized ferrites are shown in Fig. 3. The XRD spectra of both $CuFe_2O_4$ and $CoFe_2O_4$ suggested their face-centred cubic structures, referring to JCPDF 25-0283 and JCPDF 03-0864. The XRD spectrum of $Ca_2Fe_2O_5$ showed an orthorhombic crystal referring to JCPDF 38-0408. It's clear that all the strongest peaks identified in XRD patterns of prepared ferrites were fitted well with the associated JCPDF card. Therefore, the most primary component of the samples was confirmed $CuFe_2O_4$, $CoFe_2O_4$ and $Ca_2Fe_2O_5$, respectively. However, there existed minimal impurities (CuO in comparison to JCPDF 44-0706, Fe_2O_3 in comparison to JCPDF 47–1409, $CaFe_2O_4$ in comparison to JCPDF 32-0168, and CaO in comparison to JCPDF 48–1467) in the sample of $CuFe_2O_4$ and $Ca_2Fe_2O_5$ because the loss of cations happened in preparation processes or a small quantity of cations did not enter the lattice to form crystals.

3.2. Reducibility test

The reducibility of the synthesized ferrite samples was experimentally tested by means of the H_2-TPR and the CO-TGA. As shown in Fig. 4 and Table 1, their reduction behaviours obviously differed. Among three prepared ferrites, the reduction of the spinel $CuFe_2O_4$ by H_2 and CO started at the lowest temperature around 200 °C, and followed by multiple reduction peaks (at 400 °C, 650 °C and 850 °C) in both their H_2-TPR and CO-TGA curves. This revealed that there were likely several different bonding structures of oxygen in the $CuFe_2O_4$ spinel. The peak of the reducibility curve for the sample of the $CoFe_2O_4$ spinel appeared sharp and intensive in the range of 400–700 °C. The reduction temperatures of the perovskite $Ca_2Fe_2O_5$ started as high as around 600 °C, and peaked even high close to 1000 °C, presenting a pretty broad peak in both H_2-TPR and CO-TGA curves. Under a common reduction temperature range (about 600 °C), maximum reduction rates under CO or H_2 atmosphere among three ferrites followed an order of $CoFe_2O_4 > CuFe_2O_4 > Ca_2Fe_2O_5$. Despite predominant similarity nature between the current H_2-TPR and CO-TGA studies, it's still noticeable shifts in about 50 °C drift existing in corresponding peaks of the

H_2-TPR and the CO-TGA curves, with only one exception for the first peak of $CuFe_2O_4$. Several possible reasons were likely addressed to these drifts, such as temperature calibrations of TPR and TGA instrument, reactivity with atmospheres, adsorption and enthalpy difference of H_2 and CO. These differences may not alter the overall trend of our investigation.

3.3. XPS characterizations

Results of XPS characterizations on three studied complex metal oxides are shown in Fig. 5(a) for the Fe element and Fig. 5(b) for the O element. In each core excitation for each atom, the associated main peaks are fitted with several components due to different binding energies summarized in references [52–56], reflecting different components in the fitted XPS characterization results. This is because the chemical environment of each atom can be different even for the same kind of element, and a little difference in its such atoms will lead to its different binding energies [54].

In XPS spectra of the Fe 2p region, the Fe 2p core levels were split into 2p3/2 and 2p1/2. As shown in Fig. 5(a), the Fe states were characterized by an asymmetric 2p3/2 main peak, an asymmetric 2p1/2 main peak and a 2p3/2 satellite. Although both 2p3/2 and 2p1/2 peaks should have satellites, 2p1/2 satellite peaks were ignorant because of the unobvious satellite related to the 2p1/2 peak in this work. Table 2 lists Fe and O core level binding energy of all three samples and the associated proportion of the component at each binding energy. For the Fe 2p3/2 excitation, binding energies between 709.4 and 709.9 eV are attributed to Fe^{2+} [54,55]. The component proportion of Fe^{2+} from high to low were found in an order of $Ca_2Fe_2O_5 > CuFe_2O_4 > CoFe_2O_4$. Referring to the maximum reduction rates, which is $CoFe_2O_4 > CuFe_2O_4 > Ca_2Fe_2O_5$, exhibited an inverse order. Clearly, the maximum reduction rates of studied samples were negatively correlated to their Fe^{2+} proportion. The existence of Fe^{2+} may be caused by the oxygen deficiency in the samples. Furthermore, the structure of these three samples showed two kinds of Fe^{3+} sites, as consistent with the fact that two components of Fe^{3+} appear in their Fe core level XPS spectra.

Fig. 5(b) shows the XPS spectra of O 1 s for three studied samples [56]. The types of oxygen components in both $CoFe_2O_4$ and $Ca_2Fe_2O_5$ were less than those in the sample of $CuFe_2O_4$ which has three O fitted peaks. Those XPS's O peaks were rationally corresponded to multiple peaks in the H_2-TPR and CO-TGA studies. For example, the H_2-TPR and CO-TGA curves of $CuFe_2O_4$ had more peaks, implying that there are more oxygen components in the sample of $CuFe_2O_4$. Oxygen atoms in different chemical environments had different binding energies, leading different reaction temperatures with H_2 and CO. Generally, oxygen elements in oxygen carriers can be classified into the lattice oxygen (denoted as O_L) and the chemisorbed oxygen (denoted as OC) [57]. The latter are likely diversified oxygen species due to interfacing to complex lattice chemical environments. The binding energies belonging to O_L of Fe-based, Co-based and Cu-based oxides were normally between 529.5–530.2 eV [58–61]. The components labelled as O_L of $CoFe_2O_4$ and $CuFe_2O_4$ were within this range, but not for $Ca_2Fe_2O_5$. The O_L peak of $Ca_2Fe_2O_5$ was 529.2 eV, within binding energies of O 1 s in Ca-based oxides (528.6–529.2 eV) [62–64]. This is because different chemical environment around O atoms in the $Ca_2Fe_2O_5$ crystal made its peak chemical shift to lower binding energy.

As shown in Table 2, the component proportion of O_L in three studied samples followed a decreasing order of $CoFe_2O_4 > CuFe_2O_4 > Ca_2Fe_2O_5$, which was again in accordance with the order of the maximum reduction rate in TGA experiments. It means that the O_L proportion was positively related to the maximum reduction rate. It is guessed that higher concentration of O_L in the lattice may cause O atoms inside to diffuse towards at a higher diffusion rate, thus a higher reduction rate. The O_C did not seem directly and easily derivative to the similar conclusion, because of more chemical components of
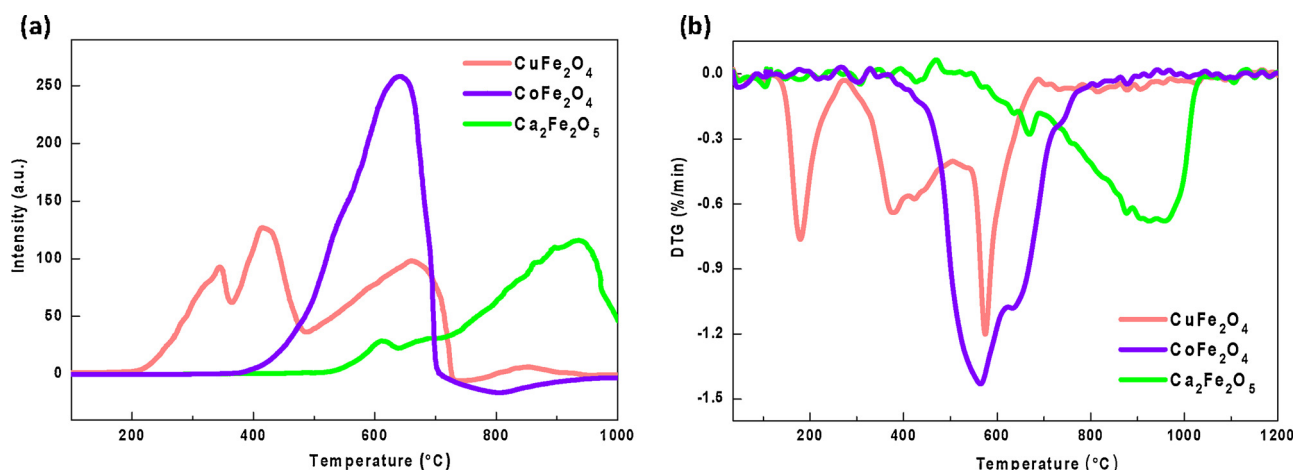
Fig. 4. Experimental results of (a) H_2-TPR and (b) CO-TGA.

Table 1
The peak temperatures for the three samples in H_2-TPR and CO-TGA experiments, respectively.

Temp.(°C)	H_2-TPR			CO-TGA		
Samples	i	ii	iii	i	ii	iii
CuFe$_2$O$_4$	360	410	660	195	390	580
CoFe$_2$O$_4$	620			580		
Ca$_2$Fe$_2$O$_5$	600	920		640	980	

O_C due to the complex chemical environment on the material surface and more bonding of O_C. However, it's rational that numbers and shapes of peaks in the H_2-TPR and CO-DTG curves were strongly related to those of the oxygen components, a single O_L and several O_C. CoFe$_2$O$_4$ and Ca$_2$Fe$_2$O$_5$ had the simplest constitution of O element (two fitted components), and correspondently, their DTG curves both showed one broaden peak with two shoulders the relatively- broad peaks corresponded to prolonged reaction time. For CuFe$_2$O$_4$, the DTG curve showed two sharp peaks and one broaden peak, corresponding to three oxygen components. To our best knowledge, O_c usually corresponds to higher binding energies compared to O_L. However, the further study is necessary to know the contribution of O_c and O_L on the reactivity in the future.

Expect for the common atoms of Fe and O in these three samples, Co, Cu and Ca also separately contribute to the fuel reduction. Ca^{2+} cannot oxidize CO/H_2 into CO_2/H_2O with itself being reduced to Ca° because Ca^{2+} has a higher reducibility than CO/H_2 [65]. However, Cu^{2+} and Co^{2+} oxides usually have high activities to convert carbon-contained fuels to be oxygen carrier [14]. The XPS for Cu 2p3/2, Cu 2p1/2, Co 2p3/2 and Co 2p1/2 are plotted in Fig. 6 and the associated information are listed in Table 3. CuFe$_2$O$_4$, and CoFe$_2$O$_4$ can exist as normal, inverse, or partially inverted spinel crystals based on the variation of cations at the tetrahedral and octahedral coordination sites [66,67]. In this study, those two compounds (CuFe$_2$O$_4$ and CoFe$_2$O$_4$) appear as the partially inverted spinel crystal since the Cu 2p and Co 2p curves both show slightly asymmetric towards higher binding energies. Both of them were fitted into two components — cations at octahedral sites and at tetrahedral sites, respectively. The main peaks of Cu 2p3/2 and Cu 2p1/2 at binding energies of 933.2 eV and 952.4 eV are assigned to Cu^{2+} at octahedral sites, while the other smaller peaks at 935.1 eV and 954.3 eV are ascribed to Cu^{2+} at tetrahedral sites [68]. Similarly, the main peaks of Co 2p3/2 and Co 2p1/2 at binding energies of 779.4 eV and 794.5 eV are assigned to Co^{2+} at octahedral sites, while the other smaller peaks at 781.4 eV and 796.1 eV are ascribed to Co^{2+} at tetrahedral sites [69]. The ratios of Cu^{2+} and Co^{2+} at octahedral

sites and at tetrahedral sites for CuFe$_2$O$_4$ and CoFe$_2$O$_4$ are 1.59 and 1.82 separately. Obviously, Cu^{2+} and Co^{2+} cations at octahedral sites with a lower binding energy is more active than ones at tetrahedral sites, and more Co^{2+} at its octahedral sites in CoFe$_2$O$_4$ compared to that of Cu^{2+} in CuFe$_2$O$_4$. Above all, it makes more sense that the reactivity with CO/H_2 in an order of CoFe$_2$O$_4$ > CuFe$_2$O$_4$ > Ca$_2$Fe$_2$O$_5$.

Furthermore, the information on particle size for the three samples have been listed in Table 4 below. As we expected, the particle size of Ca$_2$Fe$_2$O$_5$ is much smaller than that of the other two what are easy to sinter during the calcination process. As we know, particle size is usually considered as one of key factors impacting on reactivity of catalyst, especially in gas-solid reactions. However, in this study, the sample of Ca$_2$Fe$_2$O$_5$ with the largest surface area didn't perform best in the reduction with CO and H_2, which meant that other factors such as crystal structure and the percentage of lattice oxygen O_L are more dominant. CoFe$_2$O$_4$ with a slightly larger particle size than CuFe$_2$O$_4$ might contribute to the former higher reactivity on the basis of their similar crystal structure and the O_L percentage.

3.4. DFT calculations

The calculated lattice parameters are listed below in Table 5. Generally speaking, the calculated lattice parameters basically match with the referred ones, which means that it's reasonable to use our optimized structures to plot DOS and study their electronic properties.

Except for XPS core level spectra for each element, the XPS valence band spectra for the samples were also obtained, as shown in Fig. 7. XPS valence band spectra is a sort of method to visualize the occupied density of states of materials and valance electrons in the lattice [73]. Those electrons directly contribute to the bonds whose properties are the key to reactivity since electron does matter on any reaction in general. The uppermost valence band edges (VBEs) were linearly fitted by diagonal lines in blue. For the sample of CuFe$_2$O$_4$, its valence band edges crossed the Fermi level, as was consistent with the DFT calculation result as shown in Fig. 8(a). In the cases of CoFe$_2$O$_4$ and Ca$_2$Fe$_2$O$_5$, their VBEs were below but very close to Fermi level, implying that there exists a kind of nonlocal state in the band gap [74]. The fitting line of CoFe$_2$O$_4$ is more prone to be vertical than that of Ca$_2$Fe$_2$O$_5$, meaning the smaller band gap in the CoFe$_2$O$_4$ system compared to the other. This is consistent with the calculated DOS in Fig. 8(b) and (c), as well.

Fig. 8 shows the further fitting with total density of states curves (TDOS, marked in green) on the trend presenting in Fig. 7. The peak of the TDOS curve at the nearest region of its Fermi level on the left, which was a region within valance bands near its Fermi level, was marked in grey rectangles. As aforementioned, the TDOS curve crossed its Fermi level in the CuFe$_2$O$_4$ system, in highly agreement with the XPS valence
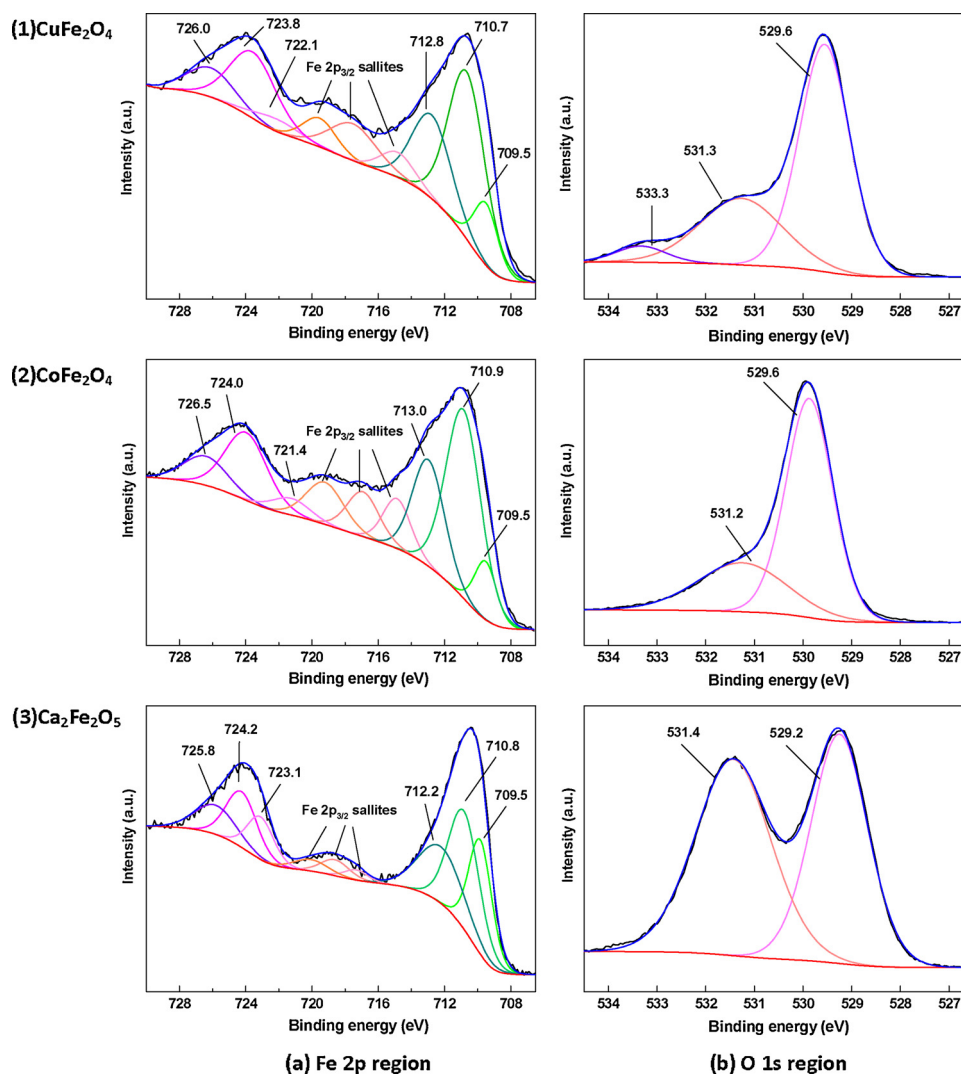
Fig. 5. XPS spectra of (a) Fe 2p and (b) O 1 s regions for (1) CuFe$_2$O$_4$, (2) CoFe$_2$O$_4$, and (3) Ca$_2$Fe$_2$O$_5$.

band spectra. It may be the reason why CuFe$_2$O$_4$ reacted earliest among the three samples in the H$_2$-TPR and CO-DTG experiments. The TDOS curve for CoFe$_2$O$_4$ got to the bottom of that peak at Fermi level, meaning a narrower band gap in this system. In the system of Ca$_2$Fe$_2$O$_5$, a wide band gap is below its Fermi level. A wider band gap below Fermi level, more difficult the electron is to be exited, therefore leading to a lower reactivity. Generally speaking, these calculated results demonstrated that the electronic structures for the calculated systems were consistent with the results of XPS characterization, as well as those of the H$_2$-TPR and the CO-TGA.

Furthermore, the partial density of state (PDOS) of p and d orbitals was also analysed in Fig. 8. Density of states for the p orbital near Fermi level was attributed to O atoms, and electrons in these orbitals occupying a higher energy band were more likely to be excited [75,76]. Obviously, O-2p bands of CuFe$_2$O$_4$ were more prone to approaching to its Fermi level. This explained why the starting temperature of the CuFe$_2$O$_4$ reduction under H$_2$ and CO was the lowest. Therefore, the approaching extents of O-2p bands to the Fermi level within valance bands (below Fermi level) were in accordance with the order of initial reducing temperatures. Consequently, both the close-to-far gap in the

Table 2
Binding energy (BE) and percentage of components of Fe 2p and O 1 s core excitation in original CuFe$_2$O$_4$, CoFe$_2$O$_4$, and Ca$_2$Fe$_2$O$_5$ by XPS characterizations.

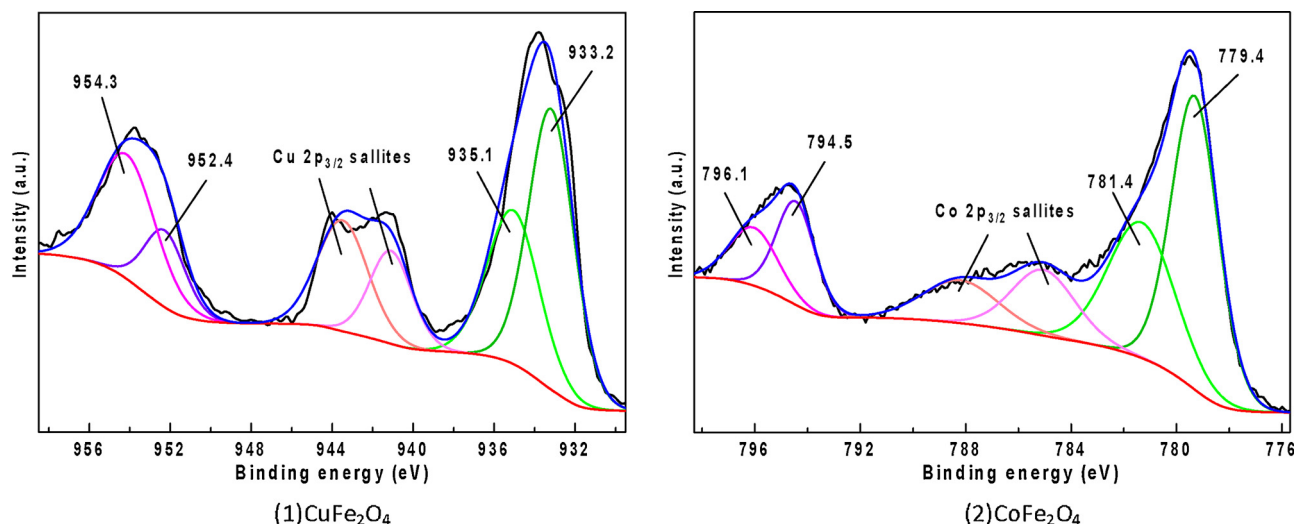| Excitation		CuFe$_2$O$_4$		CoFe$_2$O$_4$		Ca$_2$Fe$_2$O$_5$	
		BE(eV)	Percentage (%)	BE(eV)	Percentage (%)	BE(eV)	Percentage (%)
Fe 2p$_{3/2}$	Fe^{2+}	709.5	13.56	709.5	11.18	709.9	29.24
	Fe^{3+}	710.7	56.50	710.9	58.82	710.8	42.37
	Fe^{3+}	712.8	29.94	713.0	30.00	712.2	28.39
Fe 2p$_{1/2}$	Fe^{2+}	722.1		721.3		723.1	
	Fe^{3+}	723.8		724.0		724.2	
	Fe^{3+}	726.0		726.5		725.8	
O 1s	O$_L$	529.6	64.52	529.9	70.42	529.2	46.81
	O$_C$	531.3	30.97	531.2	29.58	531.4	53.19
	O$_C$	533.3	4.52				

Fig. 6. XPS spectra of Cu 2p and Co 2p for (1) $CuFe_2O_4$ and (2) $CoFe_2O_4$, respectively.

Table 3
Binding energy (BE) and percentage of components of Cu 2p and Co 2p core excitation in fresh $CuFe_2O_4$, and $CoFe_2O_4$ by XPS characterizations [68,69].

Samples		BE (eV)	BE (eV)	Percentage (%)	Ratio ($M_{oct.}^{2+}/M_{tet.}^{2+}$)
$CuFe_2O_4$		Cu $2p_{3/2}$	Cu $2p_{1/2}$		
	$Cu_{oct.}^{2+}$	933.2	952.4	61.34	1.59
	$Cu_{tet.}^{2+}$	935.1	954.3	38.65	
$CoFe_2O_4$		Co $2p_{3/2}$	Co $2p_{1/2}$		
	$Co_{oct.}^{2+}$	779.4	794.5	64.52	1.82
	$Co_{tet.}^{2+}$	781.4	796.1	35.48	

M^{2+} refers to Cu^{2+} or Co^{2+}.
tet. refers to tetrahedral sites; oct. refers to octahedral sites.

Table 4
The information on particle size for $CuFe_2O_4$, $CoFe_2O_4$, and $Ca_2Fe_2O_5$.

Terms Samples	BET Surface Area m^2/g	BJH Adsorption cumulative volume of pores cm^3/g	Adsorption average pore width nm
$CuFe_2O_4$	0.8020	0.002250	11.91582
$CoFe_2O_4$	2.4486	0.006539	11.06642
$Ca_2Fe_2O_5$	34.9417	0.076769	9.18956

O-2p band to its Fermi level and the low-to-high in initial reducing temperatures, coincided to the same trend as $CuFe_2O_4 < CoFe_2O_4 < Ca_2Fe_2O_5$. It was also found that the approaching extent of 3d bands to the Fermi level within valance bands was in accordance with the order of the maximum reduction rate in CO-TGA results: $CoFe_2O_4 > CuFe_2O_4 > Ca_2Fe_2O_5$. This may be because the position of M-3d (M: metal) bands was correlated to the diffusion rate of metal cations, which consequently influenced the diffusion rate of

lattice oxygen. Therefore, it's rational that the reduction rates of ferrites were correlated to the distributions of 3d bands within valance bands. The further simulation towards ion diffusions in ferrite systems was worth a further work.

It is noticeable that some researchers found that the $CuFe_2O_4$ performed better than $CoFe_2O_4$ in both TGA and fluidized bed experiments using pine sawdust as fuel [34]. This is because that different reductants lead to different experimental results for the performance and activity of $CoFe_2O_4$ and $CuFe_2O_4$. In our study, gaseous reductants (CO and H_2) were used to react with oxygen carriers, while solid fuel (pine sawdust) was used in the addressed literature. The big difference between these two experimental cases are the gas-solid reaction and the solid-solid reaction. The solid-solid reaction occurred in the referred literature involved the reaction of the surface oxygen on oxygen carriers in less extent with solid fuels, but in a large extent free oxygen species evolved from inner oxygen carriers. It's well known on a much higher thermodynamic tendency of CuO toward Cu_2O than Co_3O_4 toward CoO [77]. Therefore, $CuFe_2O_4$, other than $CoFe_2O_4$, can have a better performance in the case of solid fuels because of the mechanisms on the solid-solid reaction. In our case, interaction of gaseous fuels and both outer and inner surface oxygen of oxygen carriers can be feasible. Our studies exactly addressed the importance and dominant effects of the concentration of lattice oxygen (O_L) and further the percentage of cations with higher reactivity in the lattice. It's a reason why $CoFe_2O_4$ performed better than $CuFe_2O_4$ in our study, because $CoFe_2O_4$ has a higher O_L concentration and a larger percentage of cations at octahedral sites compered to $CuFe_2O_4$.

Overall, the presented DFT calculations, XPS characterization and reduction experiments were all evidently agreeable, implying that this combination approach seems promising in developing guides on predicting the properties and proposing performances of selected oxygen carriers.

Table 5
Space group, referred and calculated lattice parameters for $CuFe_2O_4$, $CoFe_2O_4$, and $Ca_2Fe_2O_5$.

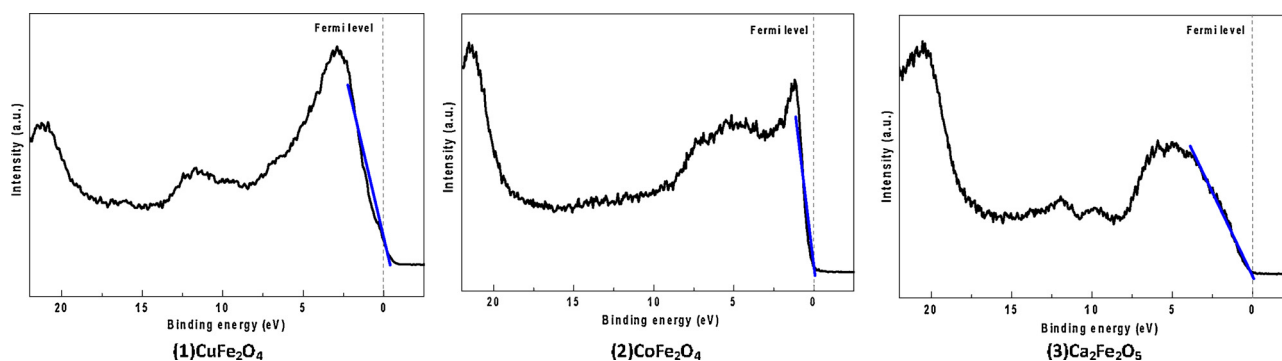| Sample	Space group	Lattice parameters											
		Referred						Calculated					
		a(Å)	b(Å)	c(Å)	α(°)	β(°)	γ(°)	a(Å)	b(Å)	c(Å)	α(°)	β(°)	γ(°)
$CuFe_2O_4$ [70]	Fd-3m	8.4	8.4	8.4	90	90	90	8.3	8.3	8.3	90	90	90
$CoFe_2O_4$ [71]	Fd-3m	8.4	8.4	8.4	90	90	90	8.2	8.2	8.2	90	90	90
$Ca_2Fe_2O_5$ [72]	PNMA	5.4	14.8	5.6	90	90	90	5.4	15.0	5.6	90	90	90

Fig. 7. XPS valance band spectra of the three samples (1) $CuFe_2O_4$, (2) $CoFe_2O_4$, (3) $Ca_2Fe_2O_5$.
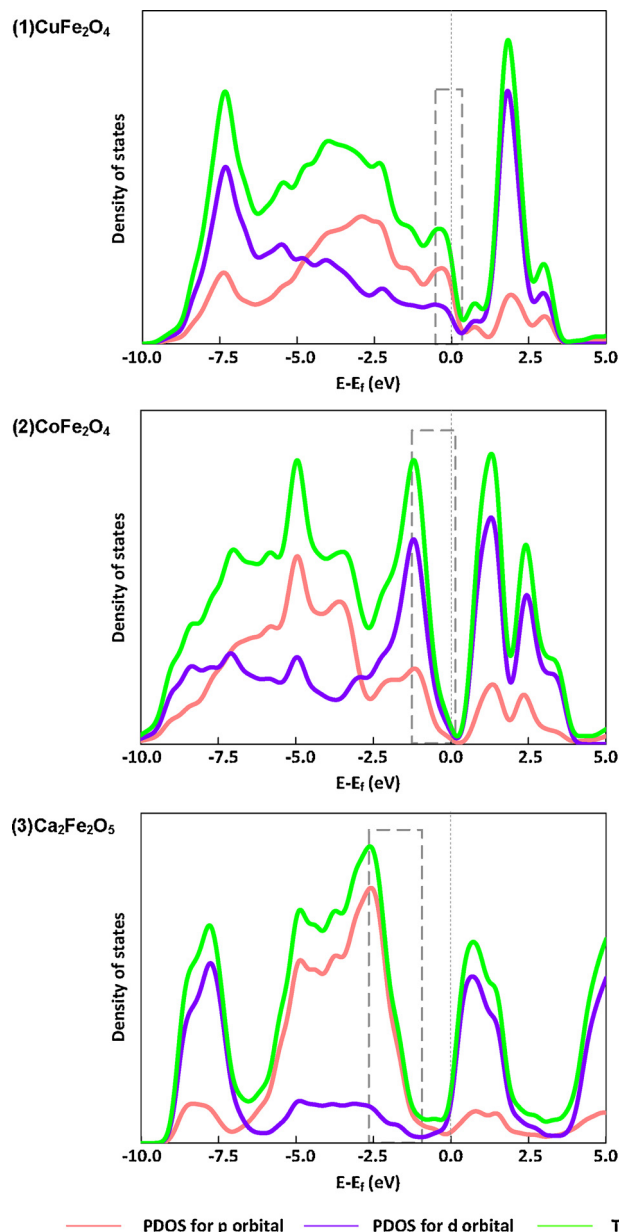

Fig. 8. Total densityof state (TDOS) in a green curve, and partial density of state (PDOS) of p and d orbitals in a purple and red curve respectively, for (1) $CuFe_2O_4$, (2) $CoFe_2O_4$, and (3) $Ca_2Fe_2O_5$ (For interpretation of the references to colour in this figure legend, the reader is referred to the web version of this article).

4. Conclusions

In the present study, three typical ferrites, such as $CuFe_2O_4$, $CoFe_2O_4$ and $Ca_2Fe_2O_5$, were synthesized by the sol-gel combustion method and characterized by XRD and XPS. Their reducibility tests were carried out using H_2-TPR and CO-TGA. DFT calculations on their geometrical optimization and electronic structure were also conducted for the associated crystal systems. It's found that results of reducibility tests were in accordance with XPS characterization and DFT calculations. This revealed that there was likely a general principle on the relationship between reducibility and electronic properties of ferrite-based oxygen carriers, leading to the following conclusive selection guidelines:

(1) The proportion of Fe^2 has a negatively effect on the reduction rate, while the proportion of lattice oxygen has a positive influence on the reducibility of ferrites.
(2) Different oxygen components in ferrites have their own characteristics of reduction behaviour such as the reacting temperature and the reduction rate.
(3) A closer approaching of the O-2p bands to Fermi level within valance bands (below Fermi level) may lead to a lower initial reducing temperature, while the approaching degree of M-3d bands to Fermi level within valance bands is positively related to the reduction rate.

Conflicts of interest

There are no conflicts to declare.

Acknowledgements

References

[1] L.S. Fan, L. Zeng, S.W. Luo, Aiche J. 61 (2015) 2–22.
[2] S.W. Luo, L. Zeng, L.S. Fan, J.M. Prausnitz (Ed.), Annual Review of Chemical and Biomolecular Engineering, vol. 6, Annual Reviews, Palo Alto, 2015, pp. 53–75.
[3] L.S. Fan, L. Zeng, W.L. Wang, S.W. Luo, Energy Environ. Sci. 5 (2012) 7254–7280.
[4] L. Qin, M.Q. Guo, Z. Cheng, M.Y. Xu, Y. Liu, D.K. Xu, J.A. Fan, L.S. Fan, J. Mater. Chem. A 5 (2017) 20153–20160.
[5] L.S. Fan, F.X. Li, Ind. Eng. Chem. Res. 49 (2010) 10200–10211.
[6] S. Bhavsar, M. Najera, R. Solunke, G. Veser, Catal. Today 228 (2014) 96–105.
[7] S.Z. Abbas, V. Dupont, T. Mahmud, Fuel 202 (2017) 271–286.
[8] M. Aghaie, M. Mehrpooya, F. Pourfayaz, Energy Conv. Manag. 124 (2016) 141–154.
[9] K. Zhao, A.Q. Zheng, H.B. Li, F. He, Z. Huang, G.Q. Wei, Y. Shen, Z.L. Zhao, Appl. Catal. B-Environ. 219 (2017) 672–682.
[10] P. Tippawan, T. Thammasit, S. Assabumrungrat, A. Arpornwichanop, Energy Conv. Manag. 124 (2016) 325–332.

[11] V.V. Galvita, H. Poelman, V. Bliznuk, C. Detavernier, G.B. Marin, Ind. Eng. Chem. Res. 52 (2013) 8416–8426.
[12] J.Z. Zhang, T. He, Z.Q. Wang, M. Zhu, K. Zhang, B. Li, J.H. Wu, Appl. Energy 190 (2017) 1119–1125.
[13] S. Liu, D. Xiang, Y. Xu, Z. Sun, Y. Cao, Appl. Energy 202 (2017) 550–557.
[14] J. Adanez, A. Abad, F. Garcia-Labiano, P. Gayan, L.F. de Diego, Prog. Energy Combust. Sci. 38 (2012) 215–282.
[15] L. Qin, A. Majumder, J.A. Fan, D. Kopechek, L.S. Fan, J. Mater. Chem. A 2 (2014) 17511–17520.
[16] Y.J. Liu, P. Kirchesch, T. Graule, A. Liersch, F. Clemens, J. Mater. Chem. A 3 (2015) 11863–11873.
[17] V.J. Aston, B.W. Evanko, A.W. Weimer, Int. J. Hydrog. Energy 38 (2013) 9085–9096.
[18] Y. Cao, A. Bianca Casenas, W.P. Pan, Energy Fuels 20 (2006) 1845–1854.
[19] Y.C. and, W.P. Pan, Energy & Fuels 20 (2006) 1836-1844.
[20] J. Motuzas, J.C.D. da Costa, J. Mater. Chem. A 3 (2015) 17344–17350.
[21] A. Abad, J. Adanez, F. Garcia-Labiano, L.F. de Diego, P. Gayan, J. Celaya, Chem. Eng. Sci. 62 (2007) 533–549.
[22] I. Martinez, R. Murillo, G. Grasa, J.R. Fernandez, J.C. Abanades, Aiche J. 59 (2013) 2780–2794.
[23] C.C. Cormos, A.M. Cormos, Int. J. Hydrog. Energy 38 (2013) 2306–2317.
[24] F. He, X. Li, K. Zhao, Z. Huang, G. Wei, H. Li, Fuel 108 (2013) 465–473.
[25] N. Galinsky, A. Mishra, J. Zhang, F.X. Li, Appl. Energy 157 (2015) 358–367.
[26] R. Bliem, E. McDermott, P. Ferstl, M. Setvin, O. Gamba, J. Pavelec, M.A. Schneider, M. Schmid, U. Diebold, P. Blaha, L. Hammer, G.S. Parkinson, Science 346 (2014) 1215–1218.
[27] J. Topfer, R. Dieckmann, G.A. Nazri, J.M. Tarascon, M. Schreiber (Eds.), Solid State Ionics Iv, Materials Research Soc, Pittsburgh, 1995, pp. 319–324.
[28] F.H. Lu, R. Dieckmann, Solid State Ion. 59 (1993) 71–82.
[29] D.G. Wickham, J. Inorg. Nucl. Chem. 31 (1969) 313–320.
[30] D.S. Mathew, R.S. Juang, Chem. Eng. J. 129 (2007) 51–65.
[31] F. Carraro, O. Vozniuk, L. Calvillo, L. Nodari, C. La Fontaine, F. Cavani, S. Agnoli, J. Mater. Chem. A 5 (2017) 20808–20817.
[32] Y.L. Kuo, W.M. Hsu, P.C. Chiu, Y.H. Tseng, Y. Ku, Ceram. Int. 39 (2013) 5459–5465.
[33] A. Evdou, V. Zaspalis, L. Nalbandian, Fuel 165 (2016) 367–378.
[34] X. Wang, Z.H. Chen, M. Hu, Y.F. Tian, X.Y. Jin, S. Ma, T.T. Xu, Z.Q. Hu, S.M. Liu, D.B. Guo, B. Xiao, Chem. Eng. J. 312 (2017) 252–262.
[35] P. Gupta, V.V. And, L.S. Fan, Energy Fuels 21 (2007) 2900–2908.
[36] S. Liu, F. He, Z. Huang, A.Q. Zheng, Y.P. Feng, Y. Shen, H.B. Li, H. Wu, P. Glarborg, Energy Fuels 30 (2016) 4251–4262.
[37] M. Rydén, A. Lyngfelt, T. Mattisson, Energy Procedia 4 (2011) 341–348.
[38] A. Lambert, C. Delqui, I. Eacute, E. Clémeneçon, V. Comte, J. Lefebvre, B. Rousseau, Durand, Energy Procedia 1 (2009) 375–381.
[39] Y. Fan, R. Siriwardane, Energy Fuels 28 (2014) 2248–2257.
[40] M. Ismail, W. Liu, M.S.C. Chan, M.T. Dunstan, S.A. Scott, Energy Fuels 30 (2016) 6220–6232.
[41] M.S.C. Chan, W. Liu, M. Ismail, Y. Yang, S.A. Scott, J.S. Dennis, Chem. Eng. J. 296 (2016) 406–411.
[42] L. Wang, L.N. Wu, C.Q. Dong, J.J. Zhang, W. Qin, Appl. Mech. Mater. 345 (2013) 298–301.
[43] Z. Cheng, L. Qin, M. Guo, J.A. Fan, D. Xu, L.S. Fan, Phys. Chem. Chem. Phys. Pccp 18 (2016) 16423.
[44] L. Qin, Z. Cheng, M. Guo, J.A. Fan, L.S. Fan, Acta Mater. (2017).
[45] C.L. Muhich, V.J. Aston, R.M. Trottier, A.W. Weimer, C.B. Musgrave, Chem. Mater. 28 (2016).
[46] F.X. Li, S.W. Luo, Z.C. Sun, X.G. Bao, L.S. Fan, Energy Environ. Sci. 4 (2011) 3661–3667.
[47] L. Qin, Z. Cheng, J.A. Fan, D. Kopechek, D. Xu, N. Deshpande, L.S. Fan, J. Mater. Chem. A 3 (2015) 11302–11312.
[48] D. Vanderbilt, Phys. Rev. B 41 (1990) 7892–7895.
[49] J.P. Perdew, K. Burke, M. Ernzerhof, Phys. Rev. Lett. 78 (1997) 1396-1396.
[50] V.I. Anisimov, J. Zaanen, O.K. Andersen, Phys. Rev. B 44 (1991) 943–954.
[51] D.X. Wu, Q.M. Zhang, M. Tao, Phys. Rev. B 73 (2006) 6.
[52] T. Yamashita, P. Hayes, Appl. Surf. Sci. 254 (2008) 2441–2449.
[53] J. Gurgul, K. Łątka, I. Hnat, J. Rynkowski, S. Dzwigaj, Microporous Mesoporous Mater. 168 (2013) 1–6.
[54] P. Mills, J.L. Sullivan, J. Phys. D Appl. Phys. 16 (2000) 723.
[55] D.D. Hawn, B.M. Dekoven, Surf. Interface Anal. 10 (2010) 63–74.
[56] N. Fang, J. Guo, S. Shu, H. Luo, Y. Chu, J. Li, Chem. Eng. J. 325 (2017) 114–123.
[57] H.Z. Chang, X.Y. Chen, J.H. Li, L. Ma, C.Z. Wang, C.X. Liu, J.W. Schwank, J.M. Hao, Environ. Sci. Technol. 47 (2013) 5294–5301.
[58] A. Gauzzi, H.J. Mathieu, J.H. James, B. Kellett, Vacuum 41 (1990) 870–874.
[59] G.F. Moreira, E.R. Peçanha, M.B.M. Monte, L.S. Leal Filho, F. Stavale, Miner. Eng. 110 (2017) 96–103.
[60] W.F. Mcclure, A. Hamid, F.G. Giesbrecht, W.W. Weeks, Appl. Spectrosc. 38 (1984) 322–329.
[61] W. Estrada, M.C.A. Fantini, S.C.D. Castro, C.N.P.D. Fonseca, A. Gorenstein, J. Appl. Phys. 74 (1993) 5835–5841.
[62] H. Ju, X. Feng, Y. Ye, L. Zhang, H. Pan, C.T. Campbell, J. Zhu, J. Phys. Chem. C 116 (2012) 20465–20471.
[63] M.I. Sosulnikov, Y.A. Teterin, J. Electron Spectros. Relat. Phenomena 59 (1992) 111–126.
[64] Y.A. Teterin, M.I. Sosulnikov, L.D. Shustov, J. Electron Spectros. Relat. Phenomena 68 (1994) 453–460.
[65] S.K. Haider, M. Erans, F. Donat, L.B. Duan, S.A. Scott, V. Manovic, E.J. Anthony, J. Energy Chem. 26 (2017) 891–901.
[66] H.S.C. Oneill, A. Navrotsky, Am. Miner. 68 (1983) 181–194.
[67] C. Reitz, C. Suchomski, J. Haetge, T. Leichtweiss, Z. Jaglicic, I. Djerdj, T. Brezesinski, Chem. Commun. 48 (2012) 4471–4473.
[68] Y. Wang, H. Zhao, M. Li, J. Fan, G. Zhao, Appl. Catal. B 147 (2014) 534–545.
[69] Z. Zhou, Y. Zhang, Z. Wang, W. Wei, W. Tang, J. Shi, R. Xiong, Appl. Surf. Sci. 254 (2008) 6972–6975.
[70] J.A. Gomes, M.H. Sousa, F.A. Tourinho, J. Mestnik, R. Itri, J. Depeyrot, J. Magn. Magn. Mater. 289 (2005) 184–187.
[71] S.M. Yunus, H. Yamauchi, A.K.M. Zakaria, N. Igawa, A. Hoshikawa, Y. Ishii, J. Alloys 454 (2008) 10–15.
[72] C.B. Vanpeteghem, R.J. Angel, J. Zhao, N.L. Ross, G.J. Redhammer, F. Seifert, Phys. Chem. Miner. 35 (2008) 493–504.
[73] D. Foix, H. Martinez, A. Pradel, M. Ribes, D. Gonbeau, Chem. Phys. 323 (2006) 606–616.
[74] G.W. Cong, W.Q. Peng, H.Y. Wei, X.X. Han, J.J. Wu, X.L. Liu, Q.S. Zhu, Z.G. Wang, J.G. Lu, Z.Z. Ye, L.P. Zhu, H.J. Qian, R. Su, C.H. Hong, J. Zhong, K. Ibrahim, T.D. Hu, Appl. Phys. Lett. 88 (2006) 062110.
[75] S.M. Xu, H. Yan, M. Wei, J. Phys. Chem. C 121 (2017) 2683–2695.
[76] S. Vázquez, L. Suescun, R. Faccio, J. Power Sources 311 (2016) 13–20.
[77] T. Mattisson, A. Lyngfelt, H. Leion, Int. J. Greenh. Gas Control. 3 (2009) 11–19.